

Phonon Thermal Transport in Silicene/Graphene Heterobilayer Nanostructures: Effect of Interlayer Interactions

Jiasheng Zhou, Haipeng Li,* Ho-Kin Tang,* Lei Shao, Kui Han, and Xiaopeng Shen*

Cite This: *ACS Omega* 2022, 7, 5844–5852

Read Online

ACCESS |



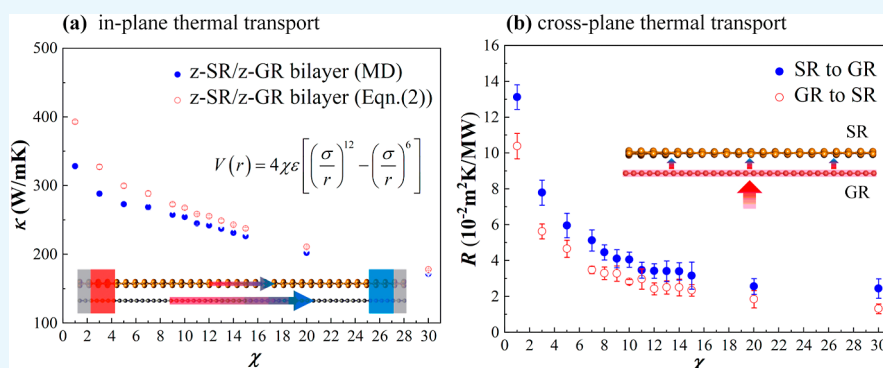
Metrics & More



Article Recommendations



Supporting Information



ABSTRACT: Heterostructuring, as a promising route to optimize the physical properties of 2D materials, has attracted great attention from the academic community. In this paper, we investigated the room-temperature in-plane and cross-plane phonon thermal transport in silicene/graphene van der Waals (vdW) heterostructures using molecular dynamics simulations. Our simulation results demonstrated that heat current along the graphene layer is remarkably larger than that along the silicene layer, which suggests that graphene dominates the thermal transport in silicene/graphene heterostructures. The in-plane phonon thermal conductivity of the silicene/graphene heterostructures could be a compromise between monolayer graphene and monolayer silicene. Heterostructuring can remarkably reduce the in-plane thermal conductivity of the graphene layer but increase the in-plane thermal conductivity of the silicene layer in heterobilayers compared with the freestanding monolayer counterparts because of their different structures. We also simulated the interlayer interaction strength effect on the in-plane phonon thermal conductivity and cross-plane interfacial thermal resistance of silicene/graphene heterostructures. Total in-plane phonon thermal conductivity and interfacial thermal resistance both decrease with the increase in the interlayer interaction strength in the silicene/graphene heterobilayers. In addition, the calculated interfacial thermal resistance shows the effect of the thermal transport direction across the interface. This study provides a useful reference for the thermal management regulation of 2D vdW heterostructures.

1. INTRODUCTION

Graphene has attracted great attention from the scientific community because of its novel physical properties, such as high mechanical strength, superior thermal conductivity, and ultrahigh carrier mobility, which make graphene a promising candidate for a wide variety of revolutionary applications in micro-electronics.^{1–3} However, its zero band gap greatly impedes its application in the semiconductor industry. Therefore, graphene is inevitably hybridized with other 2D materials when used to build field-effect transistors. Silicene, a hexagonal monolayer of silicon with a buckled structure, is of interest due to its complete compatibility with modern silicon technologies. Silicene has been fabricated using epitaxial growth on the surfaces of metal substrate and 2D materials.⁴ The first silicene-based field-effect transistors to work at room temperature (RT) have been made recently.⁵ Thus, silicene has promising application prospects in the future because of its excellent electrical properties. However, the obstacle that

hinders the application of silicene is its low thermal conductivity and mechanical strength.^{6,7} This may seriously limit the stability and performance of electronic devices. Graphene has an exceptional combination of electrical properties, high thermal conductivity, and mechanical strength; thus, these two monolayer materials can be stacked on top of each other to form an artificial heterostructure, which may tap the desirable properties of both monolayers. The atoms in different layers interact through weak van der Waals (vdW) forces. Recent studies showed that silicene on a graphene layer

Received: October 23, 2021

Accepted: February 1, 2022

Published: February 10, 2022



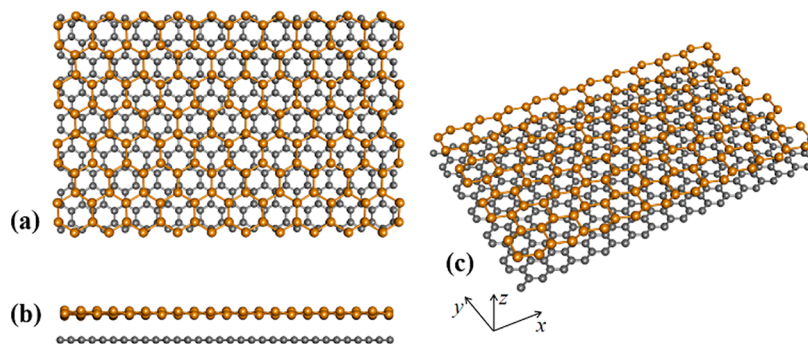


Figure 1. Schematic representation of a z-SR/z-GR heterostructure: (a) top view; (b) front view; and (c) aerial view. Yellow and gray balls represent the silicon atoms of the silicene layer and the carbon atoms of the graphene layer, respectively. The armchair edge is shown in the longitudinal direction.

or between two graphene layers can exist stably at RT because the graphene layer in the heterostructure can provide mechanical support for the silicene, and the weak interlayer interaction maintains the excellent electronic properties of silicene and graphene.^{8–10} Therefore, the silicene/graphene vdW heterostructure can be highly promising for applications in field-effect transistors, which would further require proper thermal management.

Many previous studies have reported the thermal conductivity of freestanding graphene and silicene.^{11–17} Theoretical and experimental studies have shown that the extremely high thermal conductivity of freestanding graphene is in the range of 2000–5000 W/mK near RT.^{2,18} Accurate first-principle calculations and machine learning potentials are used to study the mechanical properties and thermal conductivity of silicene nanostructures.^{19,20} The RT thermal conductivity of silicene (~ 10 – 50 W/mK^{6,15–17}) is considerably smaller than that of graphene and bulk silicon, indicating that silicene has a greater advantage in thermoelectric materials. Recently, in-plane and cross-plane thermal conductivity of heterostructures were more under discussion because of their importance in the thermal management of nanodevices. In addition, high-intensity field-effect transistors are likely to create larger heat range. Thus, it is significant to choose the type of thermal interface material in such a system.

Interfacial thermal resistance (ITR) describes the finite transmission resistance when incident phonons propagate through the interface, which is also known as thermal boundary resistance at the interface in the heterojunction. The ITR is attributed to the differences in lattice properties and scattering by the interface, which is a significant factor in heat management in many advanced applications. Although graphene is a 2D material with high thermal conductivity, the ITR still plays a critical role in dictating the overall heat transport of the graphene hybrid systems.²¹ Liu et al.²² investigated the interfacial thermal conductance of a silicene/graphene heterobilayer using molecular dynamics (MD) simulations and found that as the interface coupling strength increases, the enhanced coupling between the phonons of graphene and silicene facilitates the heat transfer between graphene and silicene and thus brings about the decrease in the ITR. Recently, Han et al.²³ calculated in-plane and out-of-plane thermal conduction of the graphene/C3N heterolayer and evaluated the effects of system size, temperature, and interlayer coupling strength on the in-plane and cross-plane thermal conductivity. The interlayer weak interaction also plays an important role in the ITR between graphene and other 2D

materials, such as graphene/hBN, graphene/stanene, graphene/MoS₂, and graphene/phosphorene vdW heterostructures.^{24–29} Particularly, for graphene hybrid monolayer and heterobilayer, the thermal conductance across the interface increases with temperature.^{22,23} Surface engineering approaches, including atomic intercalation³⁰ and chemical functionalization,^{22,31} are usually applied to tune interfacial thermal conductance. However, the effect of the interface on the in-plane thermal transport behavior of silicene/graphene vdW heterostructures is less studied in the past. In the present paper, we deposited the zigzag silicene nanoribbon (z-SR) on the zigzag graphene nanoribbon (z-GR) to model heterostructure z-SR/z-GR (Figure 1). We calculated the phonon thermal transport of silicene nanoribbon (SR) layer and graphene nanoribbon (GR) layer in the vdW heterostructure, as well as those of the freestanding monolayer SR and monolayer GR, using MD simulations. The in-plane phonon thermal conductivity and cross-plane ITR of the SR/GR heterobilayers were discussed. This study is expected to provide theoretical guidance for the regulation of thermal transport in heterostructure devices.

2. RESULTS AND DISCUSSION

2.1. In-Plane Thermal Conductivity of GR and SR Monolayers. We first calculated the values for freestanding GR and SR monolayers to benchmark our calculations with the literature. We test the width dependence of RT in-plane phonon thermal conductivity (κ) for z-SR and z-GR under periodic boundary conditions and free boundary conditions applied in the width direction, respectively. From Figure 2, we found that the boundary conditions used in the MD simulations largely affect the in-plane thermal conductivity. When the nanoribbon width increases from 2 to 12 nm, the calculated RT in-plane κ of SR and GR both increases for free boundary condition (FBC) applied in the width direction, whereas the calculated RT in-plane κ of SR and GR appears to be saturated for periodic boundary condition (PBC) in the width direction at the width greater than 4 nm. To prevent the finite-size effect in the one direction and thus to reduce the computing burden, we used PBC in the width direction for the calculations later in this paper.

Figure 3a,b displays the dependence of in-plane κ on the length (L) between the heat source and sink for freestanding z-GR and z-SR with the width of about 6 nm, respectively. Given that the L of the studied monolayer z-GR increases from 20 to 1200 nm, additional long-wavelength modes are included, and the calculated κ increases from $\sim 859.4 \pm 12.5$ to $\sim 2485.1 \pm$

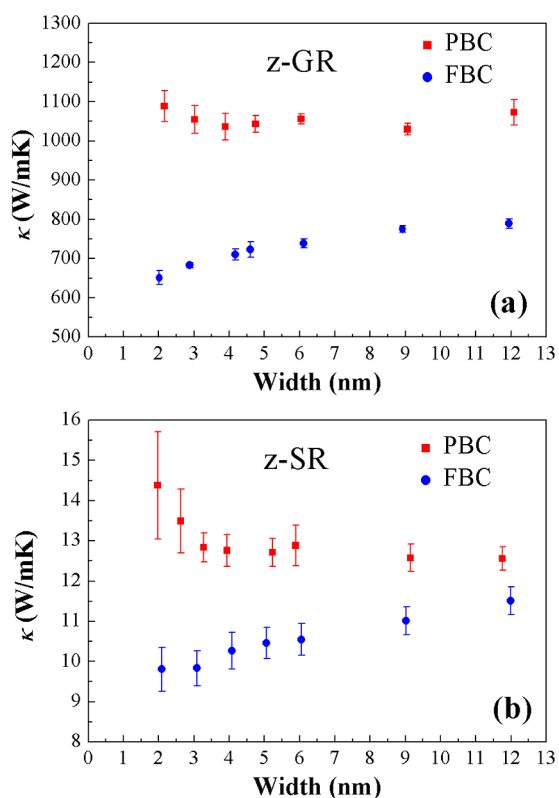


Figure 2. Width dependence of RT in-plane κ for (a) z-SR and (b) z-GR under PBC and FBC in the width direction, respectively. Here, the length (L) between the heat source and the heat sink in nanoribbon is about 40 nm.

35.9 W/mK at 300 K, consistent with the previous MD result (~ 3500 W/mK for $L = 3000$ nm).³² The calculated RT κ value of the studied GR is much lower than that of the infinite graphene (above 3000 W/mK),³³ which is due to the remarkable phonon boundary scattering induced by the limited size of atomic models for ballistic transport. Indeed, the size of the studied GR is considerably smaller than the effective phonon mean-free-path (MFP) of pristine graphene (about 775 nm at 300 K¹⁴); thus, it is not possible to incorporate the contribution of phonon modes of which MFP is much larger than the simulated domain size. Nonetheless, the calculated RT κ of freestanding z-SR increases with the increase in L from 5 to 130 nm and becomes saturated when L is larger than 20 nm. This result suggests that the effective MFP of phonon (~ 18 nm¹⁵) of silicene is comparable to the length between the heat source and sink considered here.

It is still challenging to conduct MD simulations for samples with tens of the micrometer scale. Generally, the thermal conductivity of the infinite-length nanoribbon (κ_∞) and the effective MFP (Λ) were estimated by linearly fitting the data using the following equation^{15,34}

$$\frac{1}{\kappa} = \frac{1}{\kappa_\infty} \left(1 + \frac{\Lambda}{L} \right) \quad (1)$$

It is noted that the length of the system used for fitting should be much larger than Λ in order to avoid an unphysical prediction.¹⁵ As shown in Figure 3c,d, the inverse thermal conductivity ($1/\kappa$) of the nanoribbon is linear with its inverse length ($1/L$) at the ballistic-to-diffusive regime, which is confirmed in previous studies.^{17,35} Here, at the RT κ_∞ of

silicene, the monolayer is estimated to be ~ 14 W/mK by linear fitting with the least square method, in good agreement with the previous simulation (~ 12 W/mK) reported by Zhang.¹⁵ More accurate results are recently reported using first-principles methods (20–30 W/mK;³⁶ 15–30 W/mK³⁷) and machine learning potentials (33.7 ± 0.6 W/mK,³⁸ 32.4 ± 2.9 W/mK³⁹). The underestimation of the phonon thermal conductivity by the SW potential may be due to a significant underestimation of the group velocities of the phonons around the Γ point by the SW potential as compared to the DFT results.³⁸ Moreover, our estimated κ_∞ of monolayer GR at 300 K is about 2940 W/mK, which is also close to previous theoretical and experimental results (2000–5000 W/mK^{2,18,32,40,41}) for suspended monolayer graphene.

Next, we investigated the in-plane thermal transport in the z-SR/z-GR heterostructure. The calculated κ of the z-GR layer in the z-SR/z-GR heterostructure with the same length of 40 nm is about 849.2 ± 5.2 W/mK at 300 K, which is smaller than the κ value of the same-sized freestanding z-GR (1057.6 ± 12.3 W/mK at 300 K). However, the calculated κ of the z-SR layer in z-SR/z-GR heterostructure is 23.6 ± 0.6 W/mK at 300 K, which is larger than that of the freestanding z-SR layer (12.9 ± 0.3 W/mK at 300 K). Although the thermal transport through the monolayer silicene is inefficient, the supported GR layer efficiently diffuses the heat in the heterostructure. For example, under $T = 300$ K and $\Delta T = 60$ K between the heat source and the heat sink, the major amount of heat energy in the heterostructure is transferred along the GR layer, with the heat flux along the GR layer being 20-fold higher than that along the SR layer (see Figure S1 in Supporting Information).

2.2. In-Plane Thermal Conductivity of SR/GR Heterostructures. Compared with monolayer z-GR with $L = 40$ nm ($\kappa = 1057.6 \pm 12.3$ W/mK at 300 K), the apparent reduction in the κ of the z-SR/z-GR heterostructure (by $\sim 70\%$) is because of the following two reasons. As shown in Figure 3, the κ_∞ of monolayer silicene is 2 orders of magnitude lower than that of monolayer graphene; therefore, the GR layer is the dominant thermal transport path in the heterostructure. In addition, MD simulation-predicted κ of 2D nanomaterial depends on the thickness (τ) for the nanosheet/nanofilm with the same width (i.e., $\kappa \propto 1/\tau$). In comparison, the κ of the z-SR/z-GR heterobilayer ($\sim 328.2 \pm 2.2$ W/mK) is still about 25 times the κ of freestanding monolayer z-SR with $L = 40$ nm at 300 K. This result shows that the introduction of the graphene support can remarkably enhance the heat dissipation of silicene-based electronic devices.

Because the temperature difference between the SR and GR layers is much smaller under the steady-state, interlayer heat transfer can be negligible compared to the thermal energy passing through each layer. The temperature gradients have minor differences among the SR layer, GR layer, and SR/GR bilayer, as shown in Figure S2. Since the heat flux of the bilayer heterostructure is equal to the summation of the heat flux of the silicene monolayer and graphene, the in-plane κ of the bilayer heterostructure can be approximated as follows^{42,43}

$$\kappa_{\text{bilayer}} = \frac{\kappa_{\text{GR}} \cdot \tau_{\text{GR}}}{\tau_{\text{bilayer}}} \left(1 + \frac{\kappa_{\text{SR}} \cdot \tau_{\text{SR}}}{\kappa_{\text{GR}} \cdot \tau_{\text{GR}}} \right) \quad (2)$$

It is worth noting that the composite rule of the mixture, as shown in eq 2, is only applicable when the two monolayers have strong distinct in-plane κ values. Here, the thickness of the bilayer, which is the sum of the thickness of the two

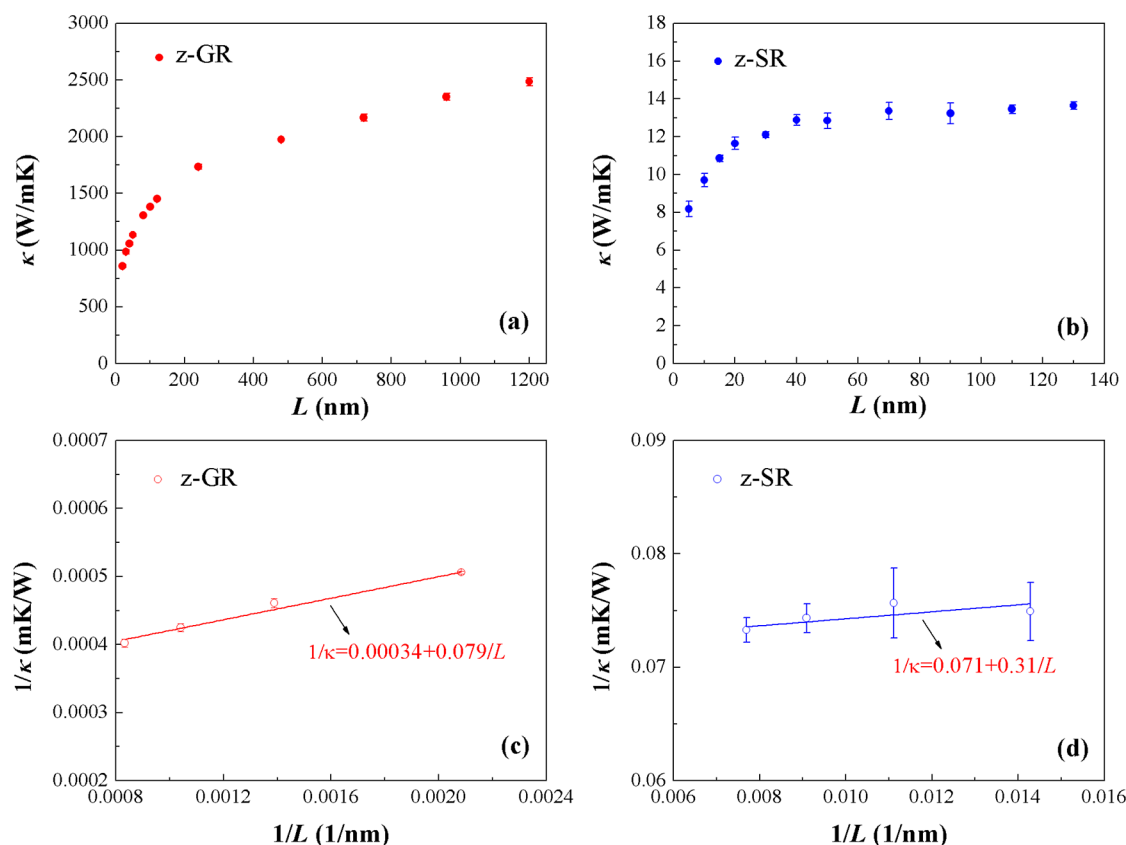


Figure 3. Length (L) dependence of RT in-plane κ of (a) z-GR and (b) z-SR monolayers, and the inverse thermal conductivity ($1/\kappa$) of (c) z-GR and (d) z-SR nanoribbons vs its inverse length ($1/L$) at the ballistic-to-diffusive regime. z-SR width = 6.03 nm, thickness = 0.42 nm; z-GR width = 6.03 nm, thickness = 0.34 nm.

monolayers, is about 2.24 times the thickness of the GR layer, that is, $\tau_{\text{bilayer}} = 2.24 \tau_{\text{GR}}$. Therefore, the total κ of the bilayer is expected to compromise between the thermal conductivity of the two monolayers.

The phonon density of states (PDOS) may reveal the variations in the internal vibration mode of a system under the impact of external factors. We calculated the PDOS using the Fourier transformation of velocity auto-correlation function in MD simulations. Figure 4 shows the total value and components of the PDOS of the SR and GR layers in the SR/GR heterostructure. The phonon frequencies of the GR layer extend up to 50 THz, whereas those in the SR layer range from 0 THz to ~ 15 THz. The large mismatch in PDOS leads to phonon Umklapp scattering,⁴⁴ which markedly lowers the total phonon thermal conductivity of the SR/GR heterostructure compared with that of GR.

2.3. Interfacial Interaction Effects on Phonon Thermal Transport in SR/GR Heterostructures. Next, we investigated the effect of the interlayer interaction strength on the in-plane and cross-plane thermal conductivity of SR/GR heterostructures. The non-bonding vdW interaction is described by $U(r) = \chi V(r)$, where $V(r)$ is the standard Lennard-Jones (LJ) potential and χ is a scaling factor used to adjust the strength of the interaction. Figure 5 shows the in-plane κ of the z-SR and z-GR layers in the SR/GR heterostructure as a function of χ , together with the total in-plane κ of SR/GR heterostructures. Interestingly, our modeled z-GR in the heterostructure with 40 nm length and about 6 nm width shows about 20% lower in-plane phonon κ at RT than that of similar-sized freestanding z-GR, whereas the room-

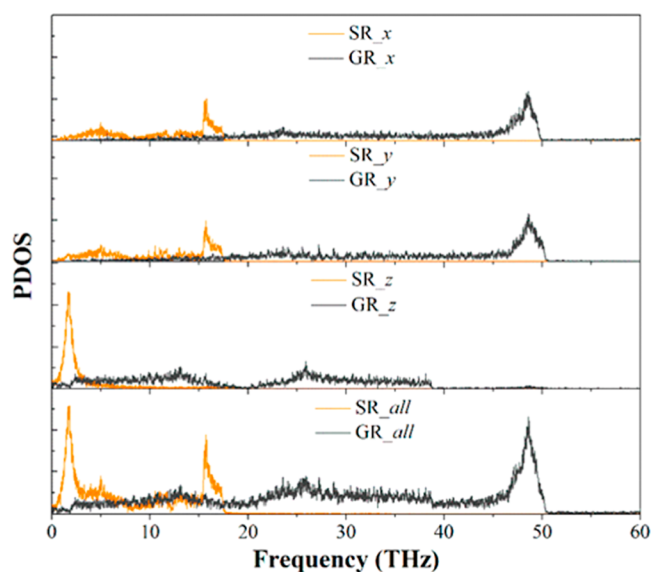


Figure 4. PDOS of z-SR and z-GR layers in the z-SR/z-GR heterostructure. Subscripts x , y , and z indicate the PDOS component along the coordinate direction, and the subscript all shows the sum of components.

temperature in-plane κ of z-SR in the heterostructure increases by about 83% compared with that of similar-sized freestanding z-SR (Figures 3 and 5). Obviously, the effect of interfacial interaction on buckled SR differs from that of flat GR. As χ increases from 1 to 30, the in-plane κ of the GR layer decreases

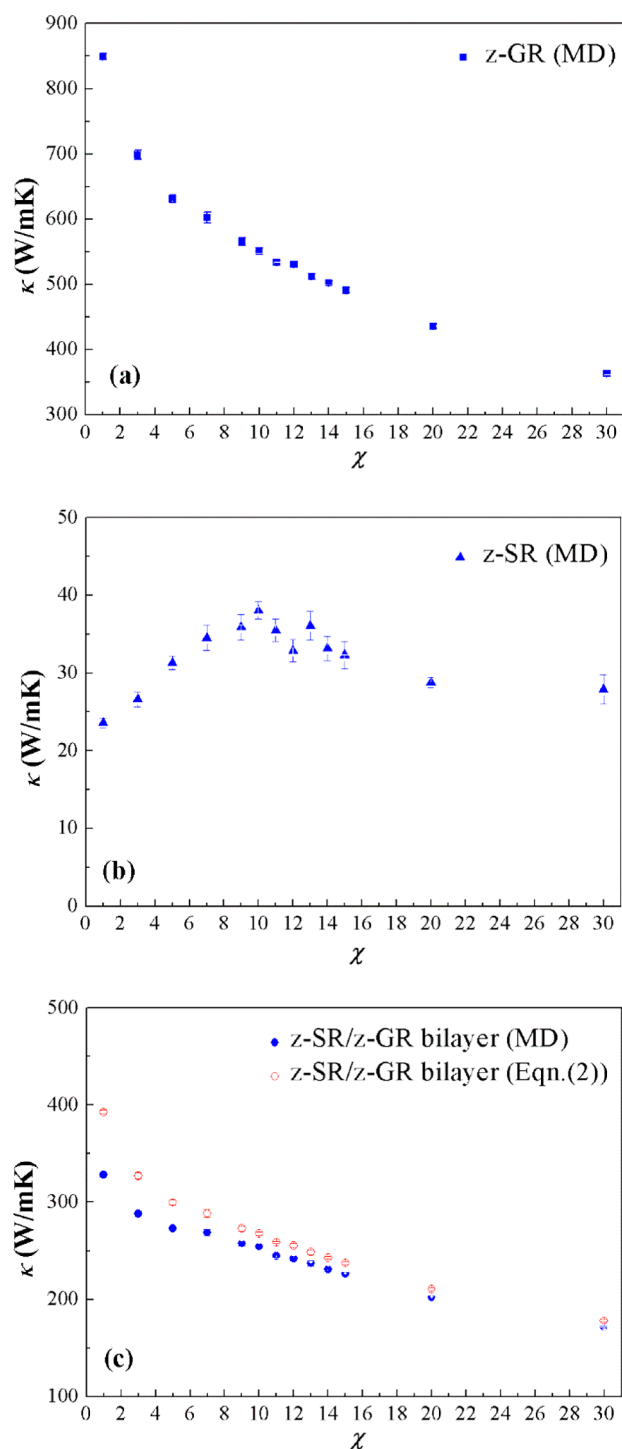


Figure 5. Effect of interfacial interaction strength (χ) on the in-plane κ of (a) z-GR layer and (b) z-SR layer in the heterostructure as compared to the (c) z-SR/z-GR bilayer. The thickness of the bilayer comes from the addition of the thickness of two monolayers. The length and width of the heterostructures are approximately 40 and 6 nm, respectively.

monotonically, whereas the in-plane κ of the SR layer increases initially and then reduces slowly after $\chi = 10$ in the SR/GR heterostructures. The special behavior of silicene can be attributed to the initial buckling structure. The introduction of the interlayer interaction, which is equivalent to the strain induced in the in-plane direction, will affect the structures of SR and GR. For the z-SR/z-GR heterostructure, the interfacial

distance between bilayers decreases with the increase in χ (Figure 6). Thus, the enhanced vdW interaction at larger χ

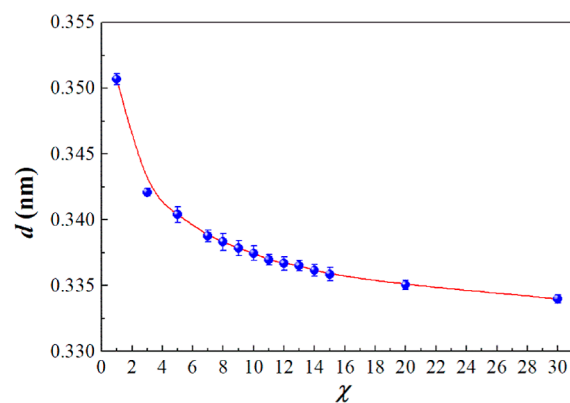


Figure 6. Dependence of interlayer distance (d) on interfacial interaction strength (χ) in the z-SR/z-GR heterostructure.

may lower the in-plane thermal conductivity of the graphene layer because of the suppressed contribution of the phonon flexural mode (ZA).⁴⁵ However, at small χ , the SR structure becomes less buckled because of bond rotation, which leads to increased in-plane stiffness and thus an increase in the thermal conductivity of the SR layer. Moreover, at large χ , Si–Si bonds are severely stretched and distorted, which decreases the in-plane stiffness and thus thermal conductivity.⁴⁶ Because the RT thermal conductivity of the silicene layer is 2 orders of magnitude smaller than that of the graphene layer, the in-plane κ of bilayer follows mostly the trend of the graphene monolayer with a variation of the χ compared to the silicene monolayer. We also found that the in-plane κ of the heterolayers predicted theoretically using eq 2 is in good agreement with the results achieved by MD calculations (Figure 5c).

ITR (R) or interfacial thermal conductance (G) describes the cross-plane thermal transport across the interface of the heterostructure. As shown in Figure 7, for $\chi = 1$ at 300 K, the ITR $R = 1/G = (13.1 \pm 0.7) \times 10^{-2} \text{ m}^2 \text{ K/MW}$ when the heat flow is from the GR layer to the SR layer and $R = (10.4 \pm 0.7) \times 10^{-2} \text{ m}^2 \text{ K/MW}$ when the heat flow is from the SR layer to the GR layer, indicating a significant effect of the thermal transport direction on the interfacial thermal conductance of

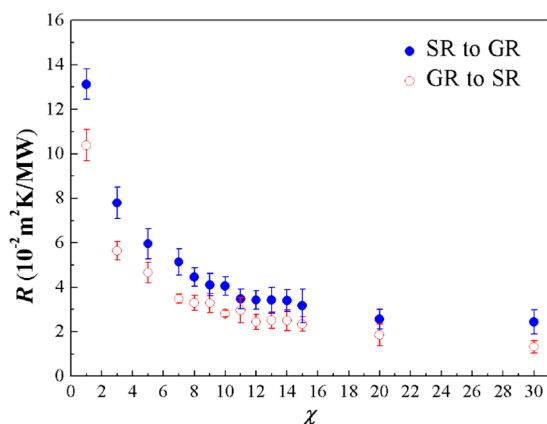


Figure 7. ITR (R) in the z-SR/z-GR heterostructures with different interfacial interaction strength (χ).

the bilayer.²⁶ We note that the calculated R also depends on the strength of the vdW coupling between the layers, consistent with previous studies of graphene-based vdW heterostructured interfaces.^{23,25–27} The ITR of silicene/graphene bilayer decreases with the increase in χ , and it shows an insignificant dependence on the heat flow direction at larger interlayer coupling strength.

3. CONCLUSIONS

MD simulations were performed to investigate the in-plane and cross-plane phonon thermal transport in silicene/graphene heterostructures. The total in-plane phonon thermal conductivity of the heterostructure is expected to compromise between the in-plane phonon thermal conductivity of two monolayers. The graphene layer is the dominant thermal transport path in the heterostructure; thus, the introduction of graphene support can remarkably enhance the heat dissipation of silicene/graphene heterostructure devices. We also simulated the effects of interlayer interaction strength on the in-plane and cross-plane phonon thermal conductivity in silicene/graphene heterostructures. When the interlayer interaction increases from 1 to 30 times, the in-plane phonon thermal conductivity of GR is remarkably decreased, but the in-plane phonon thermal conductivity of SR increases initially and then decreases slightly. However, the total in-plane phonon thermal conductivity of the heterostructure decreased with the increase in interlayer interaction strength. In addition, the calculated ITR depends not only on the strength of the vdW coupling between the layers but also on the thermal transport direction across the interface. Our study is helpful to understand the phonon thermal transport in graphene/silicene heterostructures and provides a useful reference for thermal regulation in 2D vdW heterostructures.

4. COMPUTATIONAL METHODS

The MD simulations were performed using the large-scale atomic/molecular massively parallel simulator (LAMMPS) package.⁴⁷ The Tersoff potential parameterized by Lindsay and Brodido³² was used to model the interactions between C–C bonds in the graphene layer, which can accurately describe phonon dispersion of graphene and was previously widely adopted to study the thermal and mechanical properties of graphene.^{18,24,48} The Si–Si interactions in the silicene layer were described using the optimized Stillinger–Weber (SW2) potential,¹⁵ which can provide a good description of the buckling atomic configuration of silicene.⁴⁹ The newly parameterized Stillinger–Weber (SW2) potential can well reproduce the mechanical and thermal properties of silicene nanostructures,^{15,31,49} consistent with the first-principles results and recently developed machine learning interatomic potentials.^{16,36–39,50} The non-bonding atomic interactions (i.e., vdW interactions) between the silicene and graphene layers were described by the standard LJ potential

$$V(r) = 4\epsilon \left[\left(\frac{\sigma}{r} \right)^{12} - \left(\frac{\sigma}{r} \right)^6 \right] \quad (3)$$

where r represents the interatomic distance, ϵ is the energy parameter ($\epsilon = 0.008909$ eV), and σ is the distance parameter ($\sigma = 0.3326$ nm). These parameters were previously used to model the thermal boundary conductance between SiO₂ and carbon nanotube⁵¹ and the mechanical properties of graphene/silicene/graphene heterostructures.¹⁰ The cutoff distance of

the LJ potential was set as 1.0 nm, which is about threefold of σ .

4.1. Structure Relaxation. The velocity–Verlet algorithm was used to integrate Newton's equations of motion with a time step of 0.5 fs. The silicon atoms in SR were initially displaced in a low-buckled 2D structure with a buckling distance of 0.042 nm. The average interlayer distance d was initially set to 0.36 nm, according to previous first-principles calculations.^{22,52} The lattice mismatch between SR and GR in the heterostructure was less than 5%. We apply the periodic boundary condition along the in-plane x and y directions to eliminate the edge effect. The model structures were equilibrated to obtain a steady thermal state with a successive *NPT* (constant particle number, constant pressure, and constant temperature) ensemble for 0.5 ns and *NVT* (constant particle number, constant volume, and constant temperature) ensemble for 0.5 ns by the Nosé–Hoover approach with a background temperature of 300 K. Afterward, we relaxed the system with the *NVE* (constant particles, volume, and no thermostat) ensemble for another 5 ns.

4.2. In-Plane Phonon Thermal Conductivity Calculations. Following the equilibration, the non-equilibration MD method was employed for the simulations of the in-plane phonon thermal conductivity. 0.4 nm long regions at both ends in the longitudinal direction were set as rigid walls. 5 nm long regions next to the rigid walls were set as a heat source and sink, respectively, to establish a temperature gradient along the longitudinal direction. The temperature gradient was realized using a Langevin thermostat to maintain the temperatures of the heat sink and heat source at 270 and 330 K, respectively. When non-equilibration MD simulation runs for long enough time (5–10 ns, depending on the system size), the non-equilibrium steady-state temperature distribution in the system can be obtained. The sum of added energy and subtracted energy is equal to zero, and thus, total energy is conserved. The heat flux J is computed as the energy transported per unit time across the unit area, which can be recorded by the energy (E) injection/extraction rate in the heat source/sink (see Figure S1 in Supporting Information)

$$J = \frac{dE/dt}{A} \quad (4)$$

where dE/dt is the thermal power across a cross-sectional area A .

For the 1D nanoribbon, the thermal conductivity κ of a finite system with length L is usually calculated by Fourier's law of heat conduction

$$\kappa = -\frac{J}{dT/dx} \quad (5)$$

where J is the heat flux in the longitudinal direction, and dT/dx is the temperature gradient. In this scheme, dT/dx is obtained from the slope of the so-called linear region of the temperature profile (see Figure S2 in Supporting Information), ignoring the nonlinear parts of the temperature profile near the thermal baths. This practice assumes that transport is diffusive, that is, in accordance with Fourier's law that predicts a linear temperature profile at steady-state conditions. However, thermal transport at the nanoscale, especially in materials with high thermal conductivity such as graphene, is almost ballistic with a length-dependent $\kappa(L)$.⁵³ Recent study⁵⁴ suggests that the temperature difference between the hot and cold thermostats should not exclude any local nonlinear

regions of the temperature profile in the ballistic and ballistic-to-diffusive regimes, and one should directly calculate the thermal conductance from the temperature difference (ΔT) between the hot and cold thermostats and convert it into the thermal conductivity by multiplying it with the system length (L), that is

$$\kappa = \frac{J}{\Delta T/L} \quad (6)$$

The test study shows the length dependence of κ predicted by eqs 5 and 6, respectively, shows a similar trend, and is consistent with each other near *diffusive* regimes (see Figure S3 in the Supporting Information). Considering our simulation systems with tens of the nanometer length; here, we used eq 5 to calculate κ of finite-sized GR and SR monolayers and its heterostructures.

4.3. Interfacial Thermal Resistance Calculations. With MD simulations, the thermal relaxation method is performed to calculate the ITR.^{22,23,28,31} The thermal relaxation simulations mimic the experimental pump–probe approach.⁵⁵ In the experiment, while the pump laser applies a transient heat pulse to the sample, the probe laser detects the evolution of temperature. Compared to the traditional non-equilibration MD approach, thermal relaxation simulations could not only get accurate results but also save calculation cost.⁵⁶

After the bilayer is equilibrated at 300 K, one of the layers (e.g., GR layer) is rapidly heated to a higher temperature (500 K) by velocity rescaling for 50 fs. Then, the thermostats are removed, and the layers are relaxed to the thermal equilibrium. During the thermal relaxation process, the heat is transferred from GR to SR in the form of kinetic energy and reaches a new equilibrium. Figure S4 in Supporting Information shows temperature changes of GR (T_{GR}) and SR (T_{SR}) and energy evolution of GR (E_{GR}) after introducing the 50-fs thermal impulse. The energy variation of the GR layer with time can be described by²⁸

$$\frac{\partial E_t}{\partial t} = \frac{A_{\text{interfacial}}}{R} \cdot (T_{GR} - T_{SR}) \quad (7)$$

where $A_{\text{interfacial}}$ is the interfacial area, T_{GR} and T_{SR} represent the temperature of GR and SR layer, respectively, and $\partial E_t/\partial t$ denotes the variation of GR energy with time. Then, the ITR R can be calculated from

$$E_t = E_0 + \frac{A_{\text{interfacial}}}{R} \int_0^t (T_{GR} - T_{SR}) dt \quad (8)$$

where E_0 is the initial energy of the GR layer. The linear relationship between E_t and $\int_0^t (T_{GR} - T_{SR}) dt$ is shown in Figure S5 in the Supporting Information. It should be noted that the initial data (100 ps) are excluded from the linear fitting process because of the strong energy disturbance from thermal impulse to the system at the beginning of the thermal relaxing process. We performed six independent simulations to suppress the errors.

■ ASSOCIATED CONTENT

SI Supporting Information

The Supporting Information is available free of charge at <https://pubs.acs.org/doi/10.1021/acsomega.1c05932>.

Accumulated energy to the cold bath and the subtracted energy from the hot bath as a function of simulation

time in the z-SR/z-GR heterostructure; temperature profiles in the z-SR layer, z-GR layer, and z-SR/z-GR bilayer along the x -direction for non-equilibrium MD simulation; length dependence of thermal conductivity of z-SR and z-GR; temperature evolution of the z-GR layer (T_{GR}) and z-SR layer (T_{SR}) and the energy change of the z-GR layer (E_{GR}) after introducing 50 fs thermal impulse; and E_{GR} versus the temperature difference ($T_{GR}-T_{SR}$) integration with time (PDF)

■ AUTHOR INFORMATION

Corresponding Authors

Haipeng Li – School of Materials Science and Physics, China University of Mining and Technology, Xuzhou 221116, P. R. China; orcid.org/0000-0002-3244-383X;

Email: haipli@cumt.edu.cn

Ho-Kin Tang – School of Science, Harbin Institute of Technology, Shenzhen 518055, P. R. China; Shenzhen JL Computational Science and Applied Research Institute (CSAR), Shenzhen 518129, P. R. China;

Email: denghaojian@hit.edu.cn

Xiaopeng Shen – School of Materials Science and Physics, China University of Mining and Technology, Xuzhou 221116, P. R. China; Email: xpshen@cumt.edu.cn

Authors

Jiasheng Zhou – School of Materials Science and Physics, China University of Mining and Technology, Xuzhou 221116, P. R. China

Lei Shao – Shenzhen JL Computational Science and Applied Research Institute (CSAR), Shenzhen 518129, P. R. China; Beijing Computational Science Research Center (CSRC), Beijing 100194, P. R. China; orcid.org/0000-0003-2161-5103

Kui Han – School of Materials Science and Physics, China University of Mining and Technology, Xuzhou 221116, P. R. China

Complete contact information is available at:

<https://pubs.acs.org/10.1021/acsomega.1c05932>

Notes

The authors declare no competing financial interest.

■ ACKNOWLEDGMENTS

H.L. and X.S. are supported by the Fundamental Research Funds for the Central Universities of CUMT (grant no. 2019ZDPY16) and the Six-Talent-Peaks Project in the Jiangsu Province of China (grant no. XYDXX-072). H.K. Tang is supported by the Start-Up Research Fund in HITSZ (grant no. ZX20210478 and grant no. X20220001) and Shenzhen Yuliang Technology Co., Ltd. (grant no. HX20210370). H.L. is grateful to Prof. H.Q. Lin's support for the visiting research (NSFC under grant no. 12088101). The Advanced Analysis and Computation Center of CUMT is thanked for the award of CPU hours to accomplish this work.

■ REFERENCES

- (1) Wei, Y.; Yang, R. Nanomechanics of graphene. *Natl. Sci. Rev.* **2019**, *6*, 324–348.
- (2) Balandin, A. A. Phononics of graphene and related materials. *ACS Nano* **2020**, *14*, 5170–5178.
- (3) Morozov, S. V.; Novoselov, K. S.; Katsnelson, M. I.; Schedin, F.; Elias, D. C.; Jaszczak, J. A.; Geim, A. K. Giant intrinsic carrier

- mobilities in graphene and its bilayer. *Phys. Rev. Lett.* **2008**, *100*, 016602.
- (4) Oughaddou, H.; Enriquez, H.; Tchalala, M. R.; Yildirim, H.; Mayne, A. J.; Bendounan, A.; Dujardin, G.; Ait Ali, M.; Kara, A. Silicene, a promising new 2D material. *Prog. Surf. Sci.* **2015**, *90*, 46–83.
- (5) Tao, L.; Cinquanta, E.; Chiappe, D.; Grazianetti, C.; Fanciulli, M.; Dubey, M.; Molle, A.; Akinwande, D. Silicene field-effect transistors operating at room temperature. *Nat. Nanotechnol.* **2015**, *10*, 227–231.
- (6) Li, H.-p.; Zhang, R.-q. Vacancy-defect-induced diminution of thermal conductivity in silicene. *Europhys. Lett.* **2012**, *99*, 36001.
- (7) Peng, Q.; Wen, X.; De, S. Mechanical stabilities of silicene. *RSC Adv.* **2013**, *3*, 13772–13781.
- (8) Neek-Amal, M.; Sadeghi, A.; Berdiyurov, G. R.; Peeters, F. M. Realization of free-standing silicene using bilayer graphene. *Appl. Phys. Lett.* **2013**, *103*, 261904.
- (9) Yu, S.; Li, X. D.; Wu, S. Q.; Wen, Y. H.; Zhou, S.; Zhu, Z. Z. Novel electronic structures of superlattice composed of graphene and silicene. *Mater. Res. Bull.* **2014**, *50*, 268–272.
- (10) Chung, J.-Y.; Sorkin, V.; Pei, Q.-X.; Chiu, C.-H.; Zhang, Y.-W. Mechanical properties and failure behaviour of graphene/silicene/graphene heterostructures. *J. Phys. D: Appl. Phys.* **2017**, *50*, 345302.
- (11) Wang, H.; Hu, S.; Takahashi, K.; Zhang, X.; Takamatsu, H.; Chen, J. Experimental study of thermal rectification in suspended monolayer graphene. *Nat. Commun.* **2017**, *8*, 15843.
- (12) Wei, N.; Xu, L.; Wang, H.-Q.; Zheng, J.-C. Strain engineering of thermal conductivity in graphene sheets and nanoribbons: a demonstration of magic flexibility. *Nanotechnology* **2011**, *22*, 105705.
- (13) Guo, Z.; Zhang, D.; Gong, X.-G. Thermal conductivity of graphene nanoribbons. *Appl. Phys. Lett.* **2009**, *95*, 163103.
- (14) Wang, C.; Lu, S.; Yu, X.; Li, H. Alkyl group functionalization-induced phonon thermal conductivity attenuation in graphene nanoribbons. *Chin. Phys. B* **2019**, *28*, 016501.
- (15) Zhang, X.; Xie, H.; Hu, M.; Bao, H.; Yue, S.; Qin, G.; Su, G. Thermal conductivity of silicene calculated using an optimized Stillinger-Weber potential. *Phys. Rev. B: Condens. Matter Mater. Phys.* **2014**, *89*, 054310.
- (16) Xie, H.; Hu, M.; Bao, H. Thermal conductivity of silicene from first-principles. *Appl. Phys. Lett.* **2014**, *104*, 131906.
- (17) Yu, X.; Li, H.; Zhou, J. Phonon thermal conductivity reduction in silicene nanotubes with isotope substitution. *RSC Adv.* **2020**, *10*, 10752–10757.
- (18) Nika, D. L.; Balandin, A. A. Phonons and thermal transport in graphene and graphene-based materials. *Rep. Prog. Phys.* **2017**, *80*, 036502.
- (19) Mortazavi, B.; Rahaman, O.; Makaremi, M.; Dianat, A.; Cuniberti, G.; Rabczuk, T. First-principles investigation of mechanical properties of silicene, germanene and stanene. *Phys. E* **2017**, *87*, 228–232.
- (20) Mortazavi, B.; Silani, M.; Podryabinkin, E. V.; Rabczuk, T.; Zhuang, X.; Shapeev, A. V. First-Principles Multiscale Modeling of Mechanical Properties in Graphene/Borophene Heterostructures Empowered by Machine-Learning Interatomic Potentials. *Adv. Mater.* **2021**, *33*, 2102807.
- (21) Xu, W.; Zhang, G.; Li, B. Interfacial thermal resistance and thermal rectification between suspended and encased single layer graphene. *J. Appl. Phys.* **2014**, *116*, 134303.
- (22) Liu, B.; Baimova, J. A.; Reddy, C. D.; Law, A. W.-K.; Dmitriev, S. V.; Wu, H.; Zhou, K. Interfacial thermal conductance of a silicene/graphene bilayer heterostructure and the effect of hydrogenation. *ACS Appl. Mater. Interfaces* **2014**, *6*, 18180–18188.
- (23) Han, D.; Wang, X.; Ding, W.; Chen, Y.; Zhang, J.; Xin, G.; Cheng, L. Phonon thermal conduction in a graphene-C3N heterobilayer using molecular dynamics simulations. *Nanotechnology* **2018**, *30*, 075403.
- (24) Ren, W.; Ouyang, Y.; Jiang, P.; Yu, C.; He, J.; Chen, J. The impact of interlayer rotation on thermal transport across graphene/hexagonal boron nitride van der Waals heterostructure. *Nano Lett.* **2021**, *21*, 2634–2641.
- (25) Khan, A. I.; Paul, R.; Subrina, S. Thermal transport in graphene/stanene hetero-bilayer nanostructures with vacancies: an equilibrium molecular dynamics study. *RSC Adv.* **2017**, *7*, 44780–44787.
- (26) Gong, F.; Ding, Z.; Fang, Y.; Tong, C.-J.; Xia, D.; Lv, Y.; Wang, B.; Papavassiliou, D. V.; Liao, J.; Wu, M. Enhanced Electrochemical and Thermal Transport Properties of Graphene/MoS₂ Heterostructures for Energy Storage: Insights from Multiscale Modeling. *ACS Appl. Mater. Interfaces* **2018**, *10*, 14614–14621.
- (27) Ding, Z.; Pei, Q.-X.; Jiang, J.-W.; Huang, W.; Zhang, Y.-W. Interfacial thermal conductance in graphene/MoS₂ heterostructures. *Carbon* **2016**, *96*, 888–896.
- (28) Hong, Y.; Zhang, J.; Zeng, X. C. Interlayer thermal conductance within a phosphorene and graphene bilayer. *Nanoscale* **2016**, *8*, 19211–19218.
- (29) Gu, X.; Wei, Y.; Yin, X.; Li, B.; Yang, R. Colloquium: Phononic thermal properties of two-dimensional materials. *Rev. Mod. Phys.* **2018**, *90*, 041002.
- (30) Kang, J. S.; Ke, M.; Hu, Y. Ionic intercalation in two-dimensional van der Waals materials: In situ characterization and electrochemical control of the anisotropic thermal conductivity of black phosphorus. *Nano Lett.* **2017**, *17*, 1431–1438.
- (31) Ma, H.; Babaei, H.; Tian, Z. The importance of van der Waals interactions to thermal transport in Graphene-C₆₀ heterostructures. *Carbon* **2019**, *148*, 196–203.
- (32) Lindsay, L.; Broido, D. A. Optimized Tersoff and Brenner empirical potential parameters for lattice dynamics and phonon thermal transport in carbon nanotubes and graphene. *Phys. Rev. B: Condens. Matter Mater. Phys.* **2010**, *81*, 205441.
- (33) Balandin, A. A.; Ghosh, S.; Bao, W.; Calizo, I.; Teweldebrhan, D.; Miao, F.; Lau, C. N. Superior thermal conductivity of single-layer graphene. *Nano Lett.* **2008**, *8*, 902–907.
- (34) Schelling, P. K.; Phillpot, S. R.; Keblinski, P. Comparison of atomic-level simulation methods for computing thermal conductivity. *Phys. Rev. B: Condens. Matter Mater. Phys.* **2002**, *65*, 144306.
- (35) Srinivasan, S.; Balasubramanian, G. Reduced thermal transport in the Graphene/MoS₂/Graphene heterostructure: A comparison with freestanding monolayers. *Langmuir* **2018**, *34*, 3326–3335.
- (36) Gu, X.; Yang, R. First-principles prediction of phononic thermal conductivity of silicene: A comparison with graphene. *J. Appl. Phys.* **2015**, *117*, 025102.
- (37) Xie, H.; Ouyang, T.; Germaneau, É.; Qin, G.; Hu, M.; Bao, H. Large tunability of lattice thermal conductivity of monolayer silicene via mechanical strain. *Phys. Rev. B* **2016**, *93*, 075404.
- (38) Fan, Z.; Zeng, Z.; Zhang, C.; Wang, Y.; Song, K.; Dong, H.; Chen, Y.; Ala-Nissila, T. Neuroevolution machine learning potentials: Combining high accuracy and low cost in atomistic simulations and application to heat transport. *Phys. Rev. B* **2021**, *104*, 104309.
- (39) Zhang, C.; Sun, Q. Gaussian approximation potential for studying the thermal conductivity of silicene. *J. Appl. Phys.* **2019**, *126*, 105103.
- (40) Balandin, A. A. Thermal properties of graphene and nanostructured carbon materials. *Nat. Mater.* **2011**, *10*, 569–581.
- (41) Kong, B. D.; Paul, S.; Nardelli, M. B.; Kim, K. W. First-principles analysis of lattice thermal conductivity in monolayer and bilayer graphene. *Phys. Rev. B: Condens. Matter Mater. Phys.* **2009**, *80*, 033406.
- (42) Liu, B.; Meng, F.; Reddy, C. D.; Baimova, J. A.; Srikanth, N.; Dmitriev, S. V.; Zhou, K. Thermal transport in a graphene-MoS₂ bilayer heterostructure: a molecular dynamics study. *RSC Adv.* **2015**, *5*, 29193–29200.
- (43) Rahman, M. H.; Islam, M. S.; Islam, M. S.; Chowdhury, E. H.; Bose, P.; Jayan, R.; Islam, M. M. Phonon thermal conductivity of the stanene/hBN van der Waals heterostructure. *Phys. Chem. Chem. Phys.* **2021**, *23*, 11028–11038.
- (44) Noshin, M.; Khan, A. I.; Chakraborty, R.; Subrina, S. Modeling and computation of thermal and optical properties in silicene

supported honeycomb bilayer and heterobilayer nanostructures. *Mater. Sci. Semicond. Process.* **2021**, *129*, 105776.

(45) Seol, J. H.; Jo, I.; Moore, A. L.; Lindsay, L.; Aitken, Z. H.; Pettes, M. T.; Li, X.; Yao, Z.; Huang, R.; Broido, D.; Mingo, N.; Ruoff, R. S.; Shi, L. Two-dimensional phonon transport in supported graphene. *Science* **2010**, *328*, 213–216.

(46) Pei, Q.-X.; Zhang, Y.-W.; Sha, Z.-D.; Shenoy, V. B. Tuning the thermal conductivity of silicene with tensile strain and isotopic doping: A molecular dynamics study. *J. Appl. Phys.* **2013**, *114*, 033526.

(47) Plimpton, S. Fast parallel algorithms for short-range molecular dynamics. *J. Comput. Phys.* **1995**, *117*, 1–19.

(48) Jiang, J.-W.; Lan, J.; Wang, J.-S.; Li, B. Isotopic effects on the thermal conductivity of graphene nanoribbons: Localization mechanism. *J. Appl. Phys.* **2010**, *107*, 054314.

(49) Liu, B.; Reddy, C. D.; Jiang, J.; Zhu, H.; Baimova, J. A.; Dmitriev, S. V.; Zhou, K. Thermal conductivity of silicene nanosheets and the effect of isotopic doping. *J. Phys. D: Appl. Phys.* **2014**, *47*, 165301.

(50) Mortazavi, B.; Podryabinkin, E. V.; Novikov, I. S.; Rabczuk, T.; Zhuang, X.; Shapeev, A. V. Accelerating first-principles estimation of thermal conductivity by machine-learning interatomic potentials: A MTP/ShengBTE solution. *Comput. Phys. Commun.* **2021**, *258*, 107583.

(51) Ong, Z.-Y.; Pop, E. Molecular dynamics simulation of thermal boundary conductance between carbon nanotubes and SiO₂. *Phys. Rev. B: Condens. Matter Mater. Phys.* **2010**, *81*, 155408.

(52) Hu, W.; Li, Z.; Yang, J. Structural, electronic, and optical properties of hybrid silicene and graphene nanocomposite. *J. Chem. Phys.* **2013**, *139*, 154704.

(53) Xu, X.; Pereira, L. F. C.; Wang, Y.; Wu, J.; Zhang, K.; Zhao, X.; Bae, S.; Tinh Bui, C.; Xie, R.; Thong, J. T. L.; Hong, B. H.; Loh, K. P.; Donadio, D.; Li, B.; Özyilmaz, B. Length-dependent thermal conductivity in suspended single-layer graphene. *Nat. Commun.* **2014**, *5*, 3689.

(54) Li, Z.; Xiong, S.; Sievers, C.; Hu, Y.; Fan, Z.; Wei, N.; Bao, H.; Chen, S.; Donadio, D.; Ala-Nissila, T. Influence of thermostating on nonequilibrium molecular dynamics simulations of heat conduction in solids. *J. Chem. Phys.* **2019**, *151*, 234105.

(55) Stoner, R. J.; Maris, H. J. Kapitza conductance and heat flow between solids at temperatures from 50 to 300 K. *Phys. Rev. B: Condens. Matter Mater. Phys.* **1993**, *48*, 16373–16387.

(56) Zhang, J.; Wang, Y.; Wang, X. Rough contact is not always bad for interfacial energy coupling. *Nanoscale* **2013**, *5*, 11598–11603.